Tempera paint solidification followed by single-sided NMR: an egg-cellent article that will dry you up

Floriane Gerony[a,b], Côme Thillaye du Boullay[a], Laurence de Viguerie[a], Laurent Michot[b], Pauline Martinetto[c], Maïwenn Le Denic[a], Rémi Brageu[a], Thiéry Guillou[a], Anne-Laure Rollet[b], Guillaume Mériguet[b*], Maguy Jaber[a*]

[a] Sorbonne Université, CNRS UMR 8220, LAMS, Case courrier 51, 4 pl. Jussieu, 75252 Paris, cedex 05, France
[b] Sorbonne Université, CNRS UMR 8234, PHENIX, Case courrier 225, 4 pl. Jussieu, 75252 Paris, cedex 05, France
[c] Univ. Grenoble Alpes, CNRS, Grenoble INP, Institut Néel, 38000 Grenoble, France

[*] corresponding authors

Abstract

The drying of an aqueous paint is an important criterion, since it determines not only the aesthetic aspect of the pictorial layer, but also its homogeneity and therefore the paint properties (especially its mechanical properties) and its durability over time. This article focuses on the physical drying of egg tempera paints, the most widely used technique in the Middle Ages. The egg yolk binder forms a film as it dries, which holds the pigment to the substrate. In the present study, the evaporation of water is monitored temporally and spatially using single-sided nuclear magnetic resonance (NMR), a non-invasive and non-destructive technique. Relaxometry is used to describe changes in the mobility of the different species in the yolk (mainly water and lipids) during the drying process. Inhomogeneities in the binder and paint films based on different pigments (azurite, lead-tin yellow, sienna) are highlighted. Other changes in molecular mobility are recorded on longer time scales as a result of the chemical drying of egg yolk. This study provides the first characterization of the microstructure of tempera paints during the drying process and contributes to a better understanding of this artistic technique.

Keywords: single-sided NMR, egg-tempera paint, drying, relaxometry, spatial profiling, fluid-typing

Highlights:

- Drying of paint films with and without pigments monitored by single-sided NMR
- Different ^{1}H populations have been assigned to egg yolk constituents
- Evidence of destructuring of egg yolk during drying

1 Introduction

One of the main characteristics of tempera painting is that it dries quickly. A thin layer applied with a brush to a *gesso*-type support (the most common support for painting on panels in the Middle Ages, made of gypsum and animal glue in southern Europe) dries in a few seconds. The painter therefore had to adapt his technique, applying thin layers until the desired opacity was achieved. This technique leaves no room for retouching (*pentimento*), which is why it was eventually replaced by oil paint, valued for its slower drying and greater flexibility. The way in which a layer of paint dries, influences the final characteristics of the paint, its aesthetic appearance (uniformity, cracks, etc.), its

structure and its durability (mechanical properties). It is therefore essential to study this aspect of tempera painting in order to better understand this artistic practice.

In the Middle Ages, the binder used in tempera was egg yolk, diluted slightly or greatly depending on the historical recipe [1–3]. From a physicochemical point of view, egg yolk (EY) can be considered as a natural oil-in-water emulsion [4,5]. The continuous phase is water (representing about 50 % of the total mass of EY) in which are present oil droplets (triglycerides and cholesterol) stabilized by a monolayer of proteins and phospholipids [6]. These micellar structures with a diameter of 30-70 nm are low-density lipoproteins (LDL). In addition, some proteins are solubilized in the continuous phase, and other proteins are dispersed in aggregated assemblies, known as high density lipoproteins (HDL). They are associated with phosphoproteins and LDLs, forming larger structures named granules (0.3 – 2 µm) [7]. Tempera drying is therefore a physical process, due to the evaporation of water (unlike the chemical drying of oil paint, which dries after a few years). Once solidified, the paint binder later undergoes an oxidation process similar to the drying of oils, which can be thought of as chemical drying, and which in the case of tempera paint is referred to as the aging phase [8].

In this study, we delve into the drying process of tempera paint films, a subject that, to the best of our knowledge, has never been investigated before. To accomplish this, we employ single-sided NMR, a non-invasive and non-destructive technique. Its compact, portable design makes it convenient for on-site analysis, offering a practical and innovative solution for the examination of heritage materials. For instance, it has been used to study wall frescoes [9–13] and map humidity [14,15], to determine the stratigraphy of paintings [16–18] and music instruments [19], to study the degradation of contemporary plastic works of art [20–22], of paper [23] and of a wooden sarcophagus [24], or to evaluate changes after the application of a solvent when cleaning a work of art [25–28]. A recent review shows how effective this type of high-gradient NMR technique is for monitoring the drying of thin films [29]. Using polymers as an example, the authors show that this technique allows to visualize important stages that can occur during film drying, namely solvent evaporation, curing, coalescence, skin formation and diffusion/penetration.

In the present study, this technique is employed to visualize the density of protons (^{1}H) at different depths in the sample, which allows to record the evaporation of water and the reduction in film thickness. In addition, the measurement of the ^{1}H transverse relaxation time (T_2) is fast enough to be carried out during the drying process. It correlates with molecular movements in the material [30], making it possible to study changes in the mobility of binder molecules. Signal processing allows different populations to be distinguished (fluid-typing), and we use this to track the behavior of each binder species during drying.

After quantification of the water in the yolk by TGA and characterization of the yolk by NMR spectroscopy, films of binders and paints are prepared *a tempera* with different pigments (azurite, sienna, lead-tin yellow) and left to dry in the open air. At the same time, film masses are measured to quantify water loss and compared with the evolution of proton densities by single-sided NMR. Film profiles are made with different parameters depending on what is being monitored. The ^{1}H density distribution is recorded with fine resolution, while experiments with more echoes give more precise access to transverse relaxation times T_2. The mobility of the different species is compared as a function of thickness and over time (during drying and 6 months later).

2 Materials and methods

2.1 Sample preparation and drying experiment

Organic eggs of the same brand were bought from a local store and used as fresh as possible. The yolk was carefully separated from the white by passing it from one hand to the other. Then the vitelline membrane was pierced to collect only the yolk liquid. To limit variability, three yolks from the

same box were mixed and used as a single sample. Binder solutions were prepared by adding ultrapure water to obtain a tempera solution of 75 wt% egg yolk and 25 wt% ultrapure water. The paints were prepared by adding 70 % of this tempera to 30 % of pigment powder, and mixing for 3 minutes with a muller and a glass plate. Egg-oil emulsions were prepared following a protocol described in [31]. Cold-pressed linseed oil from Kremer (#73020) was used. Egg yolk, then linseed oil, were added in a vial, for a total sample mass of 5 g. Emulsification was carried out using a high-speed homogenizer (UltraTurrax T18 digital, IKA), equipped with a S18N-10G dispersing head, at a speed of 15000 rpm for a total of 90 s. Every 30 s, emulsification was stopped, and the sample was further homogenized with a spatula. These pauses also prevent the sample from heating up.

The pigments are sourced from Kremer and are labelled lead-tin yellow type I (#10100), standard natural azurite (#10200), and Italian raw sienna (#40400). The films are then produced on glass slides with a 500 µm notched homemade applicator with a 12 mm wide aperture.

2.2 NMR spectroscopy

The ^{1}H NMR spectra of liquid and dry egg yolk (EY) were recorded with a Magritek Spinsolve 60 Ultra MultiX at 62 MHz for ^{1}H and 26 °C. Thin tubes were used, in which the liquid EY was poured, or dry EY cut into small pieces was packed at the bottom of the tube. The acquisition was made with 1 scan using a $\pi/2$ pulse of 13.2 µs. Dry spectrum was shifted to match the liquid EY chemical shifts. The transverse relaxation time T_2 were measured with the Carr-Purcell-Meiboom-Gill (CPMG) pulse sequence [30,32] and the following parameters: 4 scans with a recycle delay of 4 s, an echo time of 1 ms and 26 decay steps with an increment of 19 echoes leading to a maximum delay of 500 ms. Relaxation decays were analyzed using the built-in functions of the Spinsolve software.

2.3 Mass measurements

Mass loss in egg yolk during drying was measured with a SDT-Q600 (TA Instruments) thermogravimetric analyzer. About 40 mg of liquid EY were placed in an alumina crucible and left to dry at 25 °C under an air flow of 75 mL/min. Mass loss was recorded as a function of time.

Mass losses of the binder films during drying were recorded with a digital balance reading the mass at suitable time intervals.

2.4 Low field single-sided NMR

2.4.1 Acquisition

NMR relaxometry measurements were performed with PM2 NMR-MOUSE (Magritek) connected to a Kea2 console (Magritek) and operating at a 27.63 MHz proton frequency with a static gradient of 1.63 MHz/mm allowing a maximum spatial resolution of the order of 10 µm. A high precision mechanical lift makes it possible to scan the sample by 10 µm step to determine the profile of NMR properties in the depth of the sample.

Paint films were put on top of the instrument and were covered with a large lid to prevent quick evaporation that could result into cracks. Acquisitions are launched as soon as the films are casted. Profile experiments were carried out with a CPMG sequence to compensate the effect of the large static gradient. The pulse length was 2.3 µs, the scan used 20 µm slices during 512 echoes for a total acquisition time of 30 ms. 12 scans per slice were accumulated with a recycle delay of 0.4 s so that a profile took about 5 min. Alternatively, the 50 µm resolution profiles were probed with a sequence of 4096 echoes for a total acquisition time of 160 ms. The signal obtained corresponds to an average of 4 scans with a recycle delay of 3.5 s, resulting in 14 min experiments.

Finally, additional measurements were carried out on egg/oil emulsions. Freshly prepared emulsions were stored in sealed vials (to prevent water evaporation) and placed on top of the NMR-

MOUSE. 11 slices of 20 µm thickness were scanned successively. At each depth, the measurement sequence consisted of 4096 echoes for a total acquisition time of 232 ms. 50 scans per slice were accumulated with a recycle delay of 3.5 s. The data acquired at each depth were then averaged to give a single mean relaxation signal per emulsion sample.

2.4.2 Data processing

Single-sided NMR data were processed with an inhouse Python script. Changes in outside temperature during the experiment induce significant shifts in the depth determined by the instrument [33]. A previous study shows that there is a linear dependence between temperature and measured height [34]. This shift is caused by the temperature dependence of the magnetic field generated by permanent magnets. We therefore numerically shifted the depths by setting the film/glass blade boundary (which does not change with drying, unlike the film/air interface) to the origin.

The amplitude of the ^{1}H signal was defined as the average signal over the first 5 echoes (discarding the first echo, which has a lower amplitude [33]) of the CPMG sequence corresponding to $S(t$= 0.1-0.3 ms). The loss of water was calculated by integrating the profiles.

A low-pass filter was applied to the relaxation curves with a cutoff frequency corresponding to the inverse of the duration of one echo. An inverse Laplace transform (ILT) treatment [35] with a size of T_2 distribution of Nz = 250 and regularization parameter that controls the smoothness of the distribution (α = 3) or a bi-exponential fitting were performed to determine transverse relaxation times (T_2) and probability distributions. Data obtained on egg/oil emulsions were not filtered prior to Laplace transformation, due to the high number of scans acquired which allowed a satisfactory signal-to-noise ratio.

Data have been presented using the Scientific colormap batlow [36] to avoid visual distorsion of the data and exclusion of readers with color-vision deficiencies [37].

2.5 X-rays microtomography

High-speed high-energy absorption contrast tomography was carried out on the PSICHÉ beamline of the SOLEIL synchrotron source at 28 keV (pink mode). 3000 projections were acquired with a continuous rotation over 180 degrees, each with an exposure time of 0.3 ms. The 3D reconstruction from the projections was performed using the tomodata software [38] including the correction of flat field, ring artefacts and the use of a Paganin filter [39,40]. After this step, the data is for each acquisition a stack of 900 images of 2048×2048 pixels. The voxel size is 2.829 µm. The data were analyzed using the Fiji software [41].

3 Results and discussion

3.1 Drying of egg yolk

3.1.1 Visual changes

Figure 1 illustrates the drying of an egg yolk film of 500 µm. Egg yolk (EY) has film-forming properties due to the proteins present, which coalesce and aggregate when water evaporates [42]. After application on a glass slide, evaporation of the water causes the film to dry from the edges [43–45]. A drying front and a gelation front define a darker zone corresponding to the transition between the solid film and the liquid EY. This zone is less concentrated in water than the liquid EY, resulting in a gel structure [46,47]. At the end of the drying process, the film appears homogeneous. On the surface, micro-droplets of oil are formed (see also Supplementary Information of [8]) due to the release of lipids contained in low density lipoproteins (LDL). This indicates that LDL are partially destructured at the water/air interface [48]. Among the 60 % of lipids originally present in dry egg yolk,

only a small fraction is released by destructured LDL, otherwise the film would not have this solid appearance.

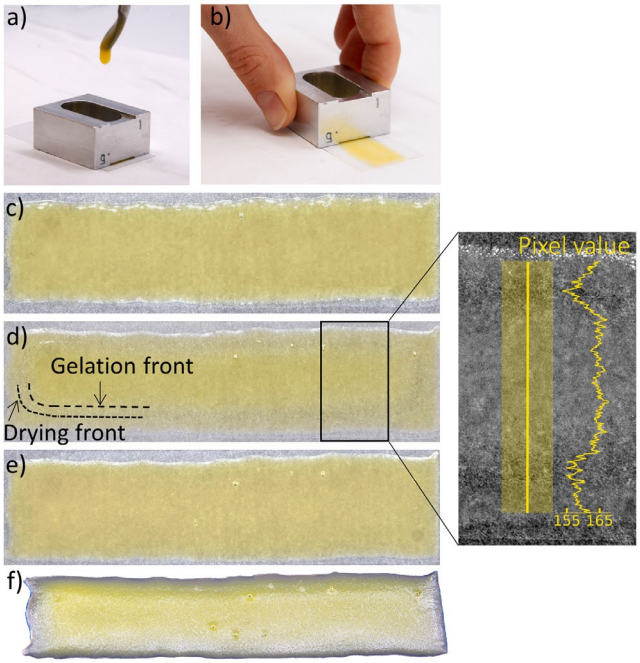

Figure 1: Drying of a film of egg yolk. (a, b) Application of the film to a glass slide. (c) Fresh film. (d) Drying film. The inset shows the greyscale image with adjusted contrast and evolution of the red component of the initial RGB image (profile averaged over a vertical band 100 pixels wide, extracted using Fiji software) showing the gelation zone between the two fronts. (e) Dry film. (f) The same dry film tilted to see the oily microdroplets covering the entire surface.

3.1.2 Composition of liquid and dry egg yolk detectable by NMR

The NMR spectrum of liquid EY shows several ^{1}H populations (Figure 2). Main peaks are attributed to water (4.8 ppm) and to CH_2 and CH_3 groups of triglycerides (at 1.2 et 0.8 ppm, respectively) [49]. The other visible peaks are assigned to triglyceride groups (Table 1), and other peaks attributed to lipid groups (triglycerides, cholesterol and phospholipids) may be visible at higher fields [50,51]. Therefore, two species are clearly detected in the egg yolk: lipids and water. No peak associated with proteins is observed because of their very low mobility in EY compounds (LDL and granules).

The spectrum of dry EY exhibits the same peaks as liquid EY excepted the one of water, confirming the previous assignment. The fatty acid peaks are still observable although their width is significantly increased. Indeed, the dipolar interactions that induces the peak broadening are no longer averaged out in the solid. This makes it more difficult to resolve them and precisely define their chemical shift.

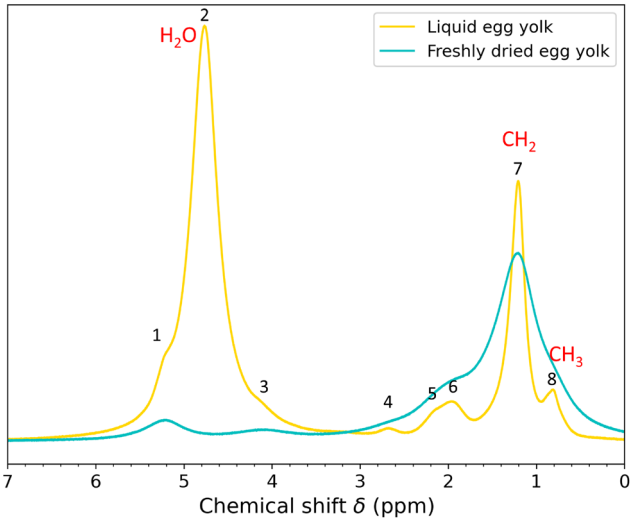

Figure 2: NMR spectra of liquid and freshly dried egg yolk.

Table 1: T_2 of liquid egg yolk obtained at 60 MHz and assignment to ^1H population [51,52].

Peak	δ(ppm)	T_2 (ms)	^{1}H assignment
1	5,2	80	Lipids
2	4,8	18	Water
3	4,2	23	Glycerol (lipids)
4	2,7	87	Fatty acids
5	2,2		CH_2 lipids
6	2	77	CH_3 lipids
7bis	1,2	60	CH_2 lipids
7	1,2	170	CH_2 lipids
8	0,8	161	CH_3 lipids

During the drying process, a loss of mass is measured, corresponding to the water naturally contained in the EY (Figure 3). The yolk contains around 50 % water [48]. This percentage may vary slightly depending on the freshness of the egg, as the vitelline membrane separating the yolk from the white becomes increasingly permeable as the days pass, and water from the white migrates into the yolk to restore the osmotic balance. We use the freshest eggs possible to limit variability. In this case, about 46 % of the initial mass is lost. In a previous study, we measured (again by TGA, but this time using a temperature ramp) about 4 % residual water after drying (loss of mass before 100 °C)[8]. This ~4 % residual water is no longer detectable by NMR spectroscopy after drying (Figure 2). The residual water may correspond to moisture which is strongly adsorbed by the dry EY [42,53]. It may also correspond to water strongly bound to the egg structures and probably to other non-visible EY structures such as proteins, whose signal is detectable by low-field NMR (see also section 3.2.3).

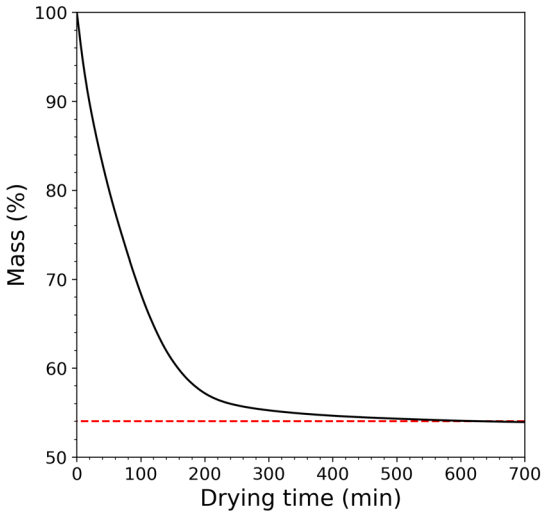

Figure 3: Mass measurements of egg-yolk during drying at 25°C under air flow (TGA).

3.2 Drying of binder films

3.2.2 ^{1}H density

We will now follow the drying of films, starting with egg yolk (Figure 4 and Figure 5) and tempera (Figure 6) samples, in order to first understand the phenomena for the pure binder and to validate the monitoring technique on a relatively simple system, before adding the various pigments. Complete drying of the film can take from a few minutes to several hours for 500 µm thick films under ambient laboratory conditions (21 °C and 40 % RH). The sensitive volume has a horizontal area of about 1 cm² [54]. 20 µm thick sections are scanned at several depths to reconstruct a stratigraphy covering the entire height of the film and a little of the air and glass slide for delimitation (Figure 4a). The amplitude of the signal is high in the film and zero in the glass slide (bottom) and air (top), making it possible to visualize the thickness and homogeneity of the film as it dries. Figure 4b shows the signal amplitude along the film depth, which is linked to the ^{1}H distribution profile. At the beginning of the experiment the film is wet, then the thickness decreases as the water evaporates from the free surface of the film. After t∼100 min, a stationary state with a constant thickness is observed. The film is considered dry. The initial thickness of EY film is about 330 µm and after drying it decreases to about 200 µm (± 30 µm because of the 20 µm resolution). The reduction in thickness is greater for tempera (Figure 6a) than for egg yolk, which is logical because it initially contains more water (about 50 % for EY and 62.5 % for tempera). The thickness of the film is decreased by about 40 % in EY and about 50 % in tempera. Considering residual water, this roughly corresponds to the water composition, so this reduction in thickness is proportional to the amount of water evaporated.

Figure 4c shows the mass loss from the whole film and the sum of the signal amplitudes at each depth, i.e. the total ^{1}H loss over the measured area of the film. Signal derivatives (Figure S1 and Figure S2) help to track the evolution of drying speeds over time. Proton loss starts after measured mass loss. It could be due to the fact that the film dries more at the film edges (not visible in the NMR) and that the diffusion fluxes of the particles in the film limit the onset of drying to the center of the film. Surprisingly, the total loss of protons is greater than the mass loss (64 % for EY instead of 41 %, and 70 % for tempera instead of 55 %). In fact, in addition to the decrease in thickness, we observed a decrease in signal amplitude at each depth between the beginning and end of drying. The proton density in oil is 5 % lower than in water based on their molar densities, which is not enough to explain the 20 % difference between mass loss and ^{1}H loss. An explanation may be that the initial amplitude of the signal is underestimated due to overly rapid relaxation of ^{1}H solids, such as proteins, which are not detected. This effect is accentuated by the fact that the overall mobility in the film decreases with

drying due to solidification, so that some of the protons fall outside the accessible experimental window (limited to relatively slow relaxations due to detection by CPMG).

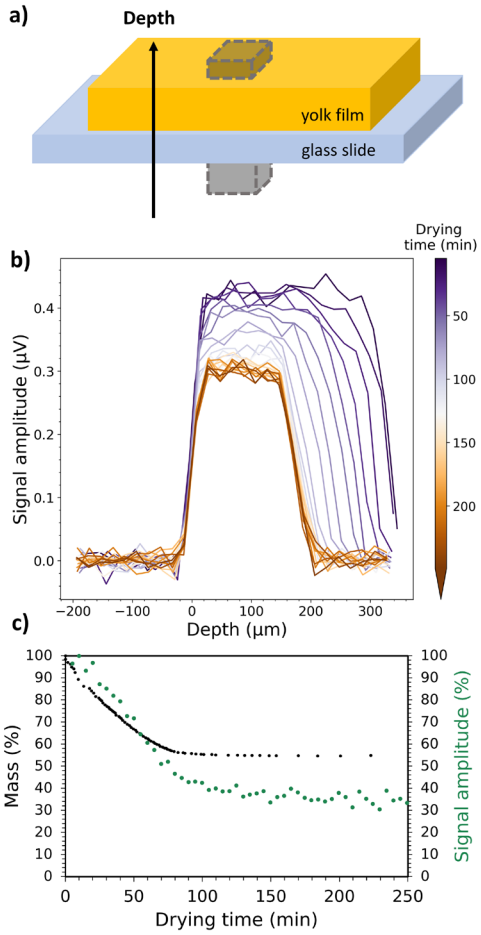

Figure 4: Drying of a yolk film. (a) Schematic representation of the volume probed, (b) ^{1}H density distribution as a function of the depth, (c) signal amplitude sum (^{1}H loss) in the sensitive volume and mass loss during drying of the film.

3.2.3 Relaxation

To study proton mobility, the complete relaxation signal is taken into account, rather than the amplitude of the signal. Since focusing on temporal evolution, lower spatial resolution and longer acquisition time are applied, going from 512 to 4096 echoes, i.e. from 30 to 160 ms. In addition, much longer recycle delays are required. All these elements lead to a critical increase in the duration of the experiments. Hence, to prevent the material from drying out too much during acquisition, the resolution is lowered and 50 µm slices are scanned instead of 20 µm slices. The signal is then averaged over the 50 µm slice(s) where it is at its maximum (selection criterion: 0.9×maximum signal) which is in the center of the film (whose position moves with drying) (Figure 5a and Figure 5b). The signal is processed with the inverse Laplace transform (ILT) to access the relaxation times (Figure 5c). To check the T_2 obtained, the signal is also fitted with a bi-exponential, which is a more robust method. The results are consistent with those obtained with ILT (Figure 5c and Figure 6c), confirming the relaxation times obtained. At the beginning of drying, three populations of protons with relaxation times of about 1 ms, 15 ms and 100 ms can be distinguished. Measurements taken at different times of the year show that, for the same egg supplier, these times and their evolution during drying vary little from one month to another (Figure S3). The evolution of the proportions of the ^{1}H populations during drying allows to attribute them to components of the egg yolk. The main peak at the beginning of drying, at $T_2 \sim 15$ ms, decreases in intensity and time until it is merged with the one at $T_2 \sim 1$ ms. It can therefore

be assigned to water, as suggested in the literature [55]. It decreases to about 1 ms as the water molecules become increasingly bound with drying. The second largest population is highly mobile (T_2 ~ 100 ms). Its concentration increases with drying. It can therefore be attributed to the lipids that gradually replace the water in the probed volume during drying, in agreement with a previous study [56]. Finally, there is a third population whose intensity is low at the beginning of the drying process and which seems to concentrate in a similar way to the lipids as the water evaporates. The relaxation time is short (T_2 ~ 1 ms), so the corresponding protons are less mobile. This population is more difficult to classify. Laghi et al (who distinguish 5 peaks) suggest assigning it to protein protons, with a small contribution from protein-lipid and protein-water interactions [55]. The latter are not very mobile due to their large size and to protein aggregation, so their contribution is not visible even at higher fields. Another possibility is that it corresponds to residual water strongly bound to the structures (including proteins). Indeed, the peak associated with water decreases with time until it reaches this population when the film is dry. This assignment is consistent with the T_2 measured at higher fields (Table 1). The T_2 of lipids is indeed longer than that of water, whose T_2 is close to that measured at low fields. This assignment challenges previous studies on egg yolk [57,58] suggesting that the most mobile population is water (without spectroscopic confirmation). This is analogous to a recent study on another complex food system, cheese, which also shows three peaks associated (from least to most mobile) with water bound to casein protein, free water, and lipids, with T_2 values comparable to ours [59].

It must be underlined that these times, measured using the NMR MOUSE, also include a diffusion contribution that should be evaluated. The measured relaxation times T_2^* is shorter than the "real" relaxation times T_2 [30] according to:

$\frac{1}{T_2^*} = \frac{1}{T_2} + \frac{D(\gamma G t_e)^2}{12}$, with T_2 the "true" transverse relaxation time, D the diffusion coefficient, γ the ^{1}H gyromagnetic ratio (267.5 $\times 10^6$ rad^{-1}.s^{-1}.T^{-1}), G the field gradient (38 T/m) and t_e the echo time (56.7 µs and 38.7 µs for experiments carried out with a spatial resolution of 20 µm and 50 µm, respectively). At the beginning of the drying, the diffusion term for lipids is very negligible as the diffusion coefficient of lipids in EY is around 10^{-11} m^2/s [52] and the equivalent apparent relaxation times $T_{2\text{-}diff}$ about 10^3 – 10^4 ms. Hence, it is not measured and $\frac{1}{T_2^*} \sim \frac{1}{T_2}$. For water, the same calculation with $D_{water}=10^{-9}$ m^2/s yields to a $T_{2\text{-}diff}$ of 50 ms. As it will be shown in the following, the diffusion contribution remains significantly weaker than the "real" relaxation. For both populations, the diffusion decreases when water evaporates and the film solidifies. At the end of the drying process, the diffusion term also becomes negligible for water and $\frac{1}{T_2^*} \sim \frac{1}{T_2}$. In consequence, diffusion does not drive the evolutions observed here, and nuclear magnetic relaxation is the predominant phenomenon.

Comparing Figure 4 and Figure 5, it appears that mass and ^{1}H losses stop before the relaxation stabilizes (~100 min *vs* ~250 min). It therefore seems that a paint that appears dry to the touch is not yet completely physically stable.

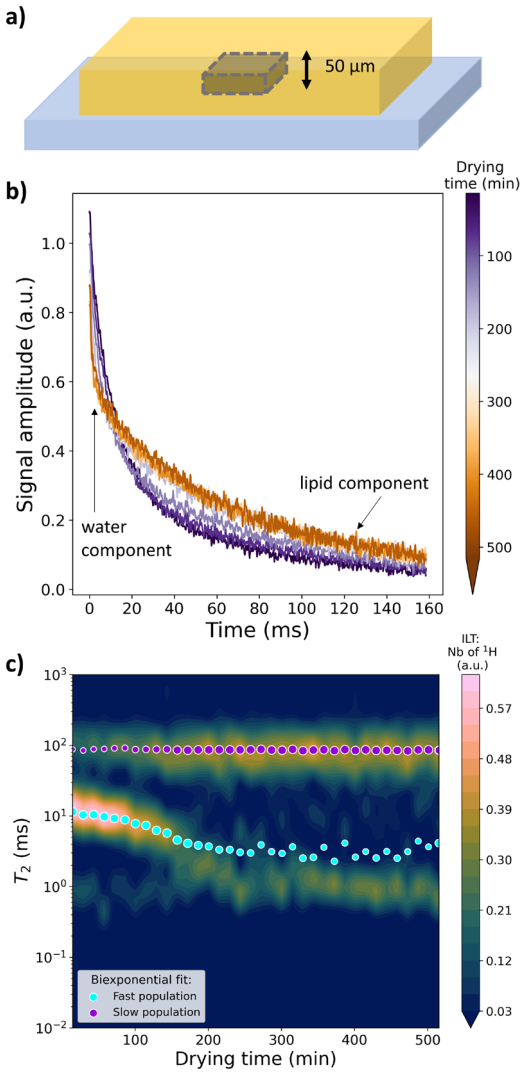

Figure 5: Evolution of molecular mobility in an egg yolk (EY) film. (a) Schematic representation of the volume probed, (b) evolution of the relaxation curves with drying, and contribution of the main EY components to the relaxation signal (c) transverse relaxation times T_2 as a function of the drying time, determined by Inverse Laplace Transform (ILT) (map) and by biexponential fit (dots). The relative ^1H number is represented proportional to the size of each dot.

The same experiment has been carried out with tempera binder. The dilution of egg yolk with water causes a change in appearance. The yolk becomes milky, reflecting a microscopic change and sedimentation occurs after a few hours. Thus, dilution destabilizes the emulsion [4]. However, in our low-field NMR experiments, no evidence of these phenomena is observed. The drying process is faster than sedimentation.

The EY dilution in water is in fact the inverse process of drying where water is removed and the relaxation time of the water decreases. Addition of water results in an increase in the population corresponding to T_2~15 ms, further confirming the assignment of relaxation populations. Dilution increases water diffusion, which should therefore reduce T_2^* according to the equation described in the previous paragraph. However, a longer T_2^* is measured upon water addition, proving that the observed effects are indeed those of relaxation, which prevail over those of diffusion.

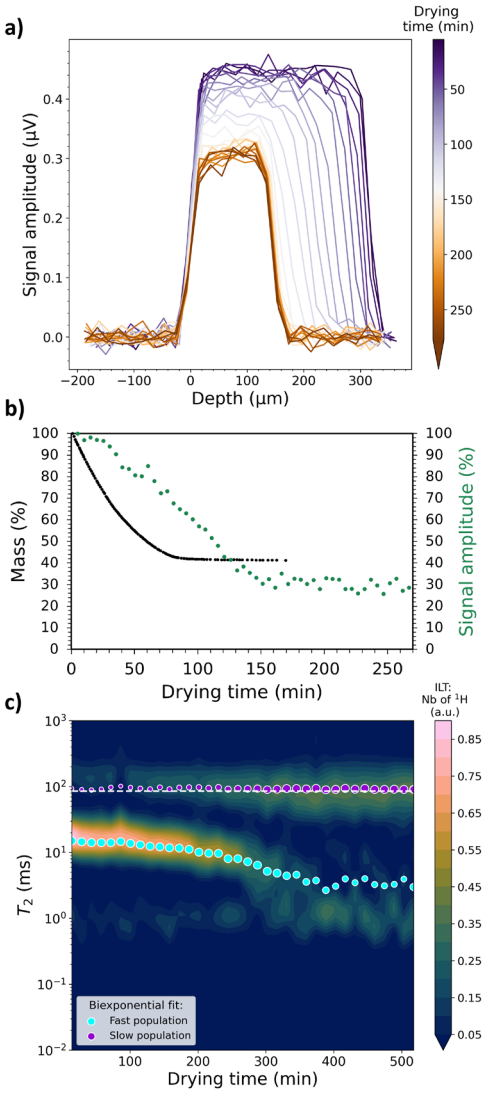

Figure 6: Drying of a tempera binder film (yolk 75 wt% / water 25 wt%). (a) ^{1}H density distribution as a function of the depth, (b) signal amplitude sum (^{1}H loss) in the sensitive volume and mass loss during drying of the film, (c) transverse relaxation times T_2 determined by Inverse Laplace Transform (ILT) (map) and by biexponential fit (dots). The relative ^{1}H number is represented proportional to the size of each dot. The white dashed line represents the lipid T_2 measured in pure egg yolk.

Similarly, when oil is added to egg yolk in emulsions (Figure 7), we observe an increase in the proportion of the population with the longest T_2, and a decrease of the two populations woth shorter T_2. This also confirms the previous attribution of the more mobile population to oil protons. Moreover, the addition of oil seems to cause a slight asymmetry of the peak (shoulder towards the longer T_2), which would indicate that oil lipids are more mobile than EY lipids. This would be consistent with the fact that egg lipids are contained in LDL lipoproteins. However, it is difficult to discriminate between the lipids originating from egg or oil in an egg /oil mixture, which is in agreement with high-field NMR measurements [50]. This is likely due to the closeness in fatty acid composition between egg yolk and linseed oil [60,61]. Therefore, fatty tempera (where the binder is a mixture of egg yolk and oil) and conventional tempera (pure egg yolk) cannot be differentiated.

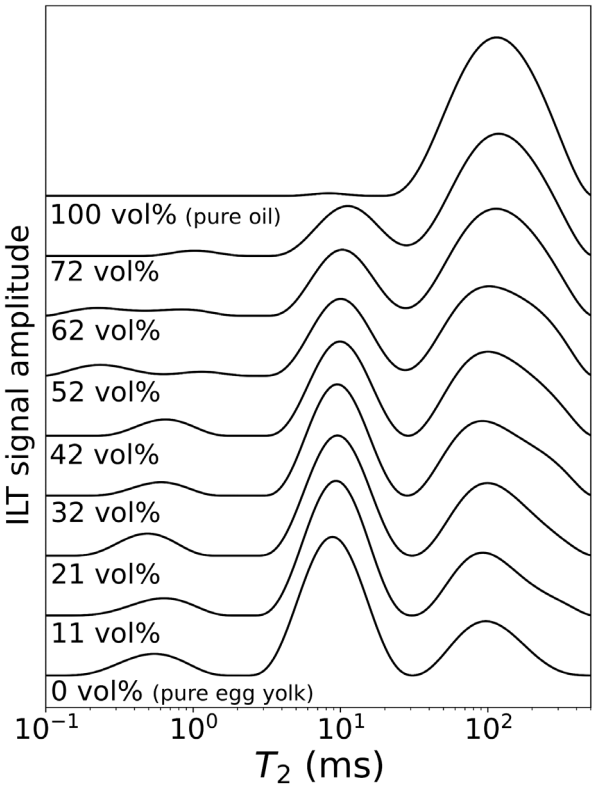

Figure 7: Inverse Laplace Transform (ILT) signal of egg/oil emulsions as a function of oil addition. The ILT signal amplitude is offset for better display.

3.2.4 Film homogeneity

The egg yolk dry film appears homogeneous in depth according to the images obtained by X-ray microtomography (Figure 8a). Similarly, the overall ^{1}H density of the previously shown films of EY (Figure 4) and of tempera (Figure 6) seems fairly homogeneous. Nevertheless, if one considers each population separately, i.e. water and lipids, the picture does not seem so homogeneous (Figure 9), especially in the case of tempera.

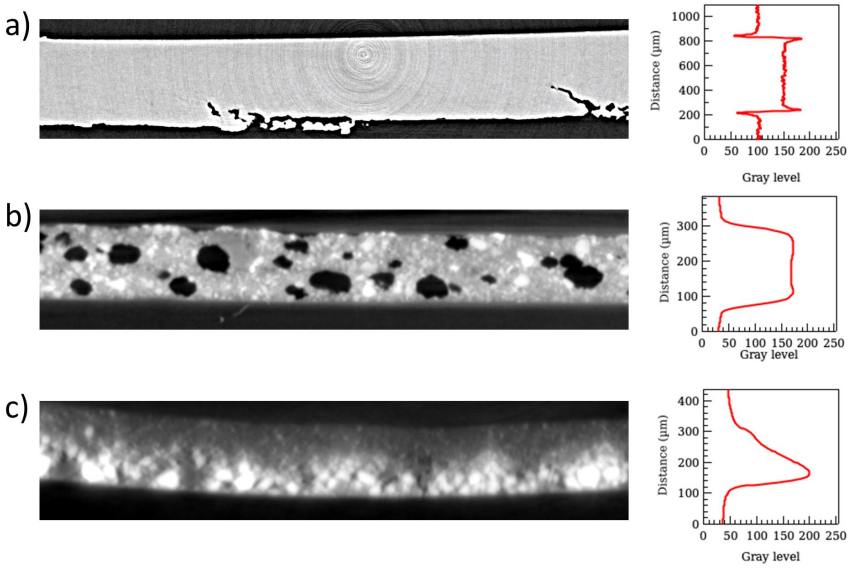

Figure 8: Tomography of slices of tempera paint films, orientated with surface in contact with air on top and in contact with substrate on the bottom: (a) yolk binder, (b) sienna, (c) azurite. The graphs show the evolution of the gray level along the depth of the films.

Figure 9 allows to distinguish between water ^{1}H and lipid ^{1}H distributions in binder films. The third ^{1}H population with the shortest T_2 (Figure 5) is discarded because too noisy and weak in intensity to distinguish any reliable evolution with drying. Also, the ILT was previously used to identify the number of ^{1}H populations, and a more robust treatment, a biexponential fitting, is used in the next section. The population labeled "slow" is that of lipids and "fast" is that of water. The following interpretations are based on the tempera film, which dries more slowly and allows a higher signal-to-noise ratio, but remain valid for the egg yolk film.

As already seen on Figure 4 and Figure 6 for the global ^{1}H density, Figure 9 shows a similar thickness evolution for both proton populations during the drying process. In other words, there is no vertical segregation of the two constituents. The intensity of the water decreases as expected due to evaporation, leading to a simultaneous enrichment of the lipid content of the film. The final intensities of egg yolk and tempera converge towards similar values for both ^{1}H density and relaxation rate. No significant effect of the initial dilution can be seen on the final state of the film.

As no significant segregation of constituents is observed, transport mechanisms should be at play to homogenize the film. At the surface, evaporation would induce water depletion accompanied by a gradient of water content in the film, drawing water from the bottom of the sample towards the surface. An inverse gradient corresponding to lipid enrichment at the surface and migration towards the bottom of the sample is also expected. Although the data are noisy due to the practical limitations of the setup, a hint of this phenomenon seems to emerge for the density profiles of water and lipids in the tempera mixture. Further confirmation of this hypothesis is required. In any case, the small gradients observed indicate efficient transport of constituents during the drying process.

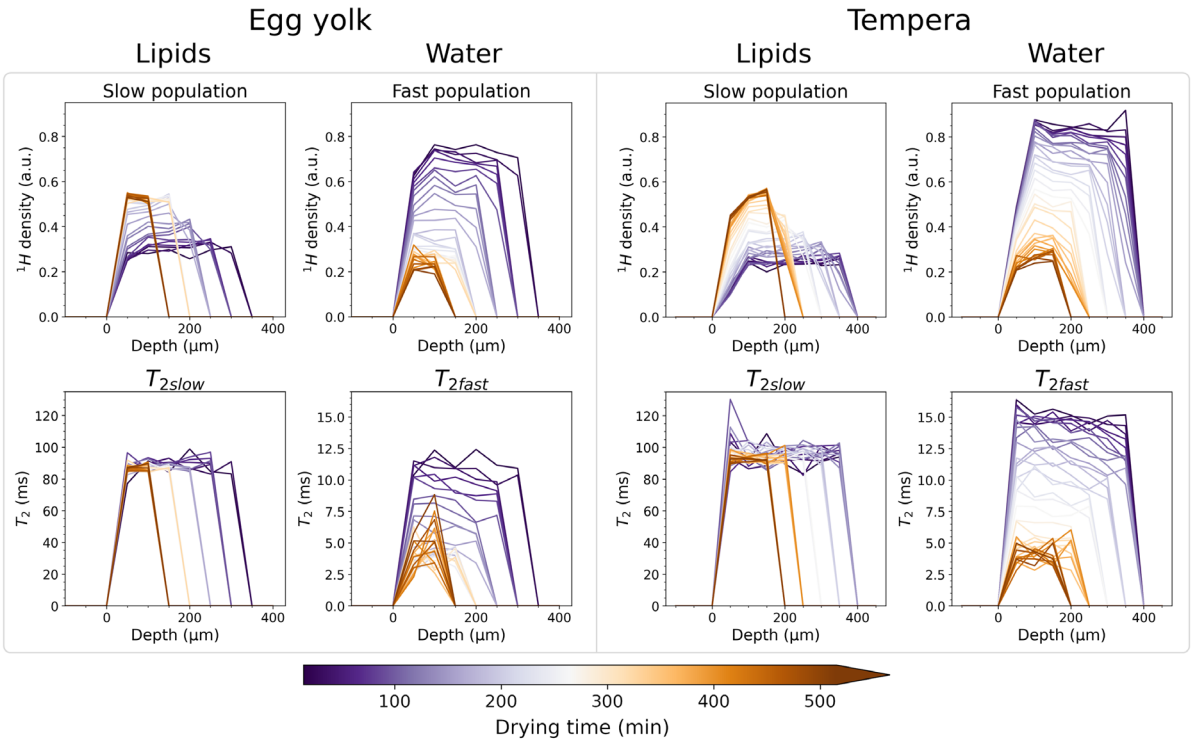

Figure 9: Lipid and water ^{1}H distributions and corresponding T_2 in a yolk film (left) and a tempera film (right).

3.3 Drying of pigmented films

The pigments used in this study are lead-tin yellow, azurite and sienna. They were characterized by XRD, SEM and pycnometry; the results are available in Supplementary Information.

Synthetic lead-tin yellow is nearly pure (Figure S4) with relatively spherical particles 0.2 to 1 µm in diameter (Figure S5), and has a density of 8.1. Azurite is a ground natural stone, and thus contains more phases. In addition to the mineral azurite (~50 %), clays (kaolinite and muscovite) are present at 40 %, and quartz completes the composition (Figure S6). The SEM images show particles that are highly dispersed in size, measuring up to several tens of microns (Figure S7). Sienna is also derived from natural earth, and contains a number of minerals, including a high proportion of clays (45 % kaolinite and smectite) and iron oxides (25 % goethite) [62].

The paints prepared with lead-tin yellow and azurite sediment quite rapidly (Figure 10). Two phases are clearly visible: dense pigment particles at the bottom, and a binder-rich phase above. In the case of lead-tin yellow, its density (8.1) induces an important sedimentation. In the case of azurite, the lower phase has an intense blue hue and contains the largest and densest particles (azurite and quartz with tabulated mineral densities of 3.8 and 2.7, respectively). The upper phase has a greyish hue. The clays particles, the lightest and smallest mineral of this pigment, are expected to be present in it, but their roughly white color cannot yield greyish tempera. Hence, the upper phase must contain also small-sized azurite particles. The sienna-based preparation appears visually much more homogeneous.

Figure 10: Preparations of tempera paints with (from left to right) lead-tin yellow, azurite and sienna a few moments after being poured into flasks: sedimentation is observed in the first two flasks.

X-ray tomography experiments provide information about the homogeneity of the dry films in depth (Figure 8). The heavy elements, corresponding to the pigments, are visible in light contrasts. On the other hand, phases with low absorption, such as the binder, are in light gray, and the darkest phases correspond to air bubbles. It was not possible to analyze the lead-tin yellow film because of the X-rays absorption and fluorescence of tin (K edge 29.2 keV) falls in the energy range of the pink beam. Sienna film appears relatively homogeneous after drying, with numerous inclusions and bubbles trapped in the binder. Azurite film presents, similarly to the liquid paint shown in Figure 10, strong heterogeneity in the pigment distribution within the depth. The largest particles are concentrated at the bottom of the film, covered by a layer of smaller particles. Small particles can be seen all over the film but we cannot identify their nature (azurite, kaolinite or muscovite). In this way, despite tempera being a fast-drying paint, films formulated with dense mineral pigments are not homogeneous in thickness, with the pigments concentrated on the substrate surface and covered by egg yolk. It suggests that the painter application method is important for such paint, as the visual aspect should be different between a homogenous pigmented film and a film with the pigments laid on the medium and covered by the EY binder. In addition, sedimentation followed by drying causes inhomogeneities in the cohesion of the film, resulting in mechanical stresses, as evidenced by the curvature of the azurite film (Figure 8).

To go further and monitor the changes during drying, the ^{1}H distribution profiles have been recorded for the three pigments (Figure 11 - top). The general appearance of graphs based on azurite and sienna is very different from that of tempera alone. The first profile, measured in 5 minutes, is already strongly inhomogeneous, showing that sedimentation is fast. This was expected for azurite according to Figure 8 and Figure 10, but wasn't for sienna.

The profile of the lead-tin yellow paint appears homogeneous, except that the lowest layer, just above the one on the glass slide surface, has a lower ^{1}H density, which must correspond to the volume mainly occupied by the sedimented pigment. This aspect is further commented in the Supplementary information section (Figure S8). The thickness of the sedimentation layer is very thin, about 10-20 µm. It is consistent with the facts that the particles are very dense and are very small in size, consequently occupying a small thickness in relation to the total volume of the suspension. Above this layer, a similar profile as for the drying of pure tempera can be observed (Figure 6) with a globally high ^{1}H density.

The profile for the azurite pigment is more complex, with at least three zones. As for lead-tin yellow, the layer near the glass surface is less dense in ^{1}H because the volume is mainly occupied by the densest particles, azurite and quartz, that have sedimented (see also Figure S8). Just above, at the start of drying, it has a layer rich in ^{1}H and above, a less concentrated one. After drying, the stratigraphy remains the same: a binder concentration gradient is visible, and very few binder ^{1}H are present on the surface layer occupying ⅓ of the film thickness. This surprising profile seems to be caused by the heating of this sample region by the RF pulse sequences during the drying process monitoring, as shown in the Supplementary Information section (Figure S8 and Figure S9).

As for the sienna-based film, the signal amplitude is more intense in the center of the film, so the ^{1}H distribution is not homogeneous in depth. It would therefore appear that there are denser particles at the bottom, something that could not be seen in the flask or by microtomography. However, the ^{1}H localization gradient is much less pronounced than for azurite. The particles are less dense (overall density of 2.9 compared with 3.5 for azurite) and more homogeneously distributed within the film.

The signal from the ^{1}H richest region in each profile is used to extract, by Laplace transform, the T_2 of the binder components in the presence of pigments (Figure 11). Taking the zone where the signal is at its maximum, *i.e.* where the binder is the most concentrated, may lead us to consider a zone of reduced size. For example, in the case of azurite after drying, this corresponds to the signal of a single 20 µm thickness. This still allows us to measure the relaxation of at least the two main populations of yolk: water and lipids. The evolution of T_2 as a function of drying is shown in Figure 11 - bottom. The representation appears noisier because the measured signal is weaker due to the presence of the pigment, which simply reduces the ^{1}H concentration.

For lead-tin yellow, three populations are detected, and the initial T_2 values and their evolution are very similar to those observed for pure binder. In fact, the layer probed above the sedimentation layer corresponds to tempera. A very small decrease in the lipid mobility is observed. This reduction in mobility may be due to the addition of pigments which act as fillers, and has been shown for acrylic [63,64] and oil films [65].

For azurite and sienna only two ^{1}H populations can be distinguished. In addition, there is also a general decrease of the relaxation times compared to the binder alone. Both pigments contain paramagnetic elements, Fe(III) for sienna and Cu(II) for azurite, that increase the NMR relaxation rates. In consequence, the populations for which the relaxation times are close to the sampling frequency cannot be detected. The T_2 are more reduced in sienna than in azurite: the water population times decrease from around 15 ms with lead-tin yellow to 5 ms with azurite and 2 ms with sienna at the beginning of the drying. As for lipid ^{1}H, at the end of the drying, the T_2 of lipid protons is about 65 ms in the presence of lead-tin yellow, 40 ms with azurite and 20 ms with sienna (Figure 12). As previously mentioned, in egg yolk, lipids are embedded within the LDL. Therefore, in this state, they should not be affected by the Fe(III) and Cu(II) ions, as the dipolar interaction between ^{1}H and electron, that yields to the enhancement of NMR relaxation, decreases with the ^{1}H-e distance at the power 6. This could

be a sign of the partial degradation of this LDL organization and a release of the lipids, as suggested by the apparition of lipid droplets at the surface of the film after drying.

A decrease in water mobility is also observed as the films dry, similar to that observed with the binder alone (Figure 4 and Figure 6).

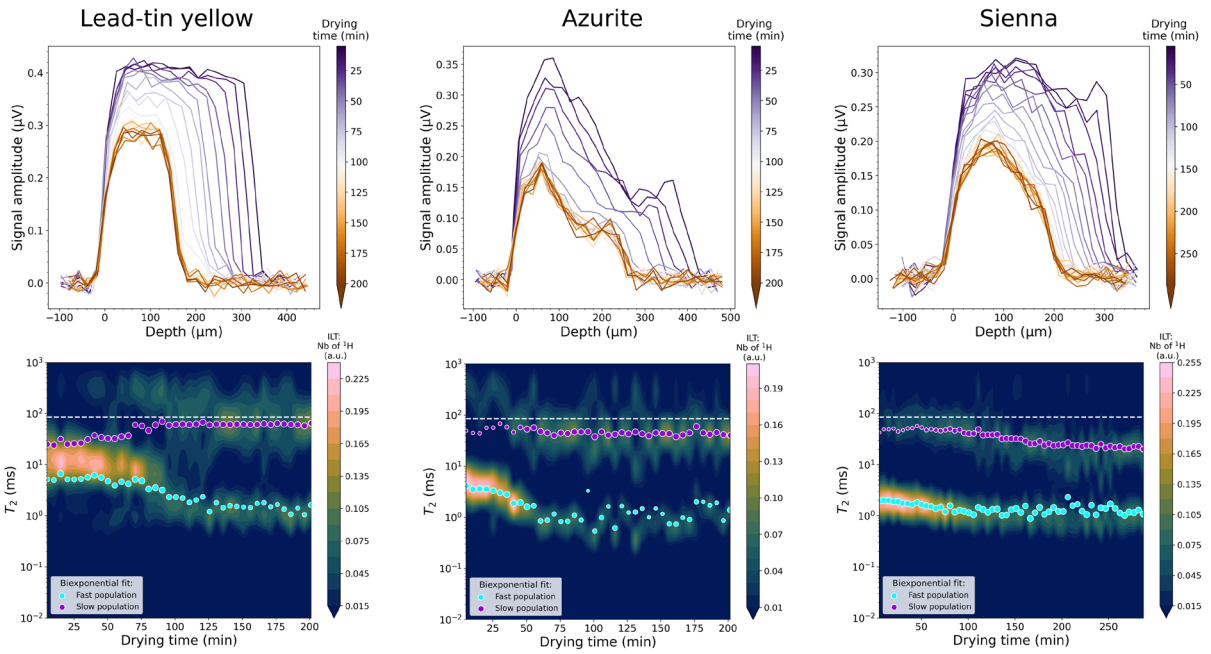

Figure 11: Drying of paint films. (top) ^{1}H distribution profiles and (bottom) transverse relaxation times T_2 as a function of the drying time, determined by Inverse Laplace Transform (ILT) (map) and by biexponential fit (dots). The relative ^{1}H number is represented proportional to the size of each dot. The white dashed line represents the lipid T_2 measured in pure egg yolk.

3.4 Chemical drying (aging)

The relaxation times collected previously show that at the end of the drying process of the binders and paints, the film contains highly mobile lipids (T_2~100 ms in binder films) and therefore liquid lipids. Residual water, possibly bound to proteins, is also detected. Lipids that are mobile after drying do not remain so indefinitely. Figure 12 shows the evolution of the T_2 transverse relaxation times of lipids ^{1}H after 6 months of natural aging. A significant decrease in lipid mobility can be observed in each film. This can be explained by the fact that the lipids undergo chemical drying, similar to the drying of oils, by oxidation with air dioxygen promoted by light [4,8,66,67]. Solidification of the film by lipid cross-linking is therefore measured. This curing effect, which leads to a decrease in T_2, has also been demonstrated by single-sided NMR on acrylic and oil films with different pigments [68]. The effect seems greater in the presence of pigment, which was also demonstrated in a previous study [8]. In addition, a discoloration is observed in pure binder and azurite films (Figure S9).

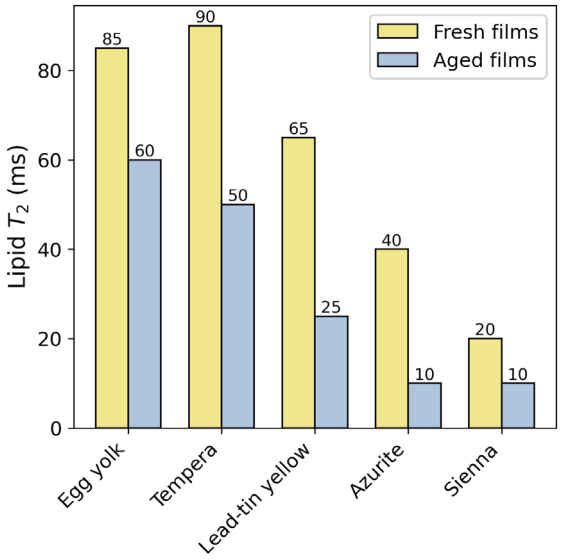

Figure 12: Lipid T_2 relaxation times in freshly dried films (fresh films) and after six months of natural aging (aged films).

4 Conclusion

The drying of binder films and egg tempera paint with different pigments was monitored using single-sided NMR, a non-invasive and non-destructive technique. This technique makes it possible to monitor the kinetics of the phenomenon and to determine the composition and mobility profiles with depth. Drying induces a significant reduction in the thickness of the binder films correlated to the amount of water evaporated and consistent with the loss of mass over time. Binder films are relatively homogeneous in thickness, whereas the pigment particles can induce sedimentation, which complicates stratigraphy. For binder films, this study shows a relatively homogeneous drying of the film with a decrease in the water content and its mobility together with an increase in the lipid content whose mobility seems to be little affected by the process. Thus, after physical drying, the films consist of very little water, strongly bound to the protein structure, and highly mobile lipids. When pigments are added, relaxation rates measurements indicate a decreased mobility, suggesting an interaction between the lipids and the pigments. For longer periods of time, chemical drying induces a decrease in lipid mobility related to oxidation and reticulation processes. This study identifies and quantifies the phenomena that occur at the initial stages of drying on model systems for tempera paints. In particular, the noticeable effect of pigment addition on a rather homogeneous water-binder mixture in its absence raises many questions about the drying of films deposited on more complex substrates such as canvas or underpainting, or about brush applications of such mixtures. The sedimentation effect observed for pigment particles on a vertical substrate also needs to be addressed. Finally, one of the ultimate aims of this approach is to use this original technique, based on this portable instrument, to determine the location and state of water and binder on a real painting.

References

[1] C. De L'escalopier, Théophile Prêtre et Moine, Essai Sur Divers Arts, Libr. des Arts et métiers-Ed. J. Laget, Paris, 1977.

[2] M.P. Merrifield, ed., Medieval and Renaissance treatises on the arts of painting: original texts with English translations, Dover Publications, Mineola, N.Y, 1999.

[3] C. Cennini, Cennino Cennini's Il libro dell'arte: a new English translation and commentary with Italian transcription, Archetype Publications, London, 2015.

[4] J.J. Boon, S.L. Peulvé, O.F. van den Brink, M.C. Duursma, D. Rainford, Molecular aspects of mobile and stationary phases in ageing tempera and oil paint films, in: Early Italian Paintings - Techniques and Analysis: Symposium, Maastricht, 9 - 10 October 1996, T. Bakkenist, Stichting Restauratie Atelier Limburg, Maastricht, 1996.
[5] T. Strixner, J. Sterr, U. Kulozik, R. Gebhardt, Structural Study on Hen-egg Yolk High Density Lipoprotein (HDL) Granules, Food Biophysics 9 (2014) 314–321. https://doi.org/10.1007/s11483-014-9359-y.
[6] M. Anton, Egg Yolk Constituents and Structures, in: Handbook of Egg Science and Technology, 1st ed., CRC Press, Boca Raton, 2023: pp. 103–120. https://doi.org/10.1201/9781003254430-8.
[7] C.M. Chang, W.D. Powrie, O. Fennema, Microstructure of egg yolk, Journal of Food Science 42 (1977) 1193–1200. https://doi.org/10.1111/j.1365-2621.1977.tb14458.x.
[8] F. Gerony, L. De Viguerie, Y. Boulard, C. Thillaye Du Boullay, L. Michot, A.-L. Rollet, G. Mériguet, M. Jaber, Monitoring the aging process in egg-tempera paint films, Spectroch Acta A 328 (2025) 125371. https://doi.org/10.1016/j.saa.2024.125371.
[9] B. Blümich, F. Casanova, M. Dabrowski, E. Danieli, L. Evertz, A. Haber, M. Van Landeghem, S. Haber-Pohlmeier, A. Olaru, J. Perlo, O. Sucre, Small-scale instrumentation for nuclear magnetic resonance of porous media, New J. Phys. 13 (2011) 015003. https://doi.org/10.1088/1367-2630/13/1/015003.
[10] V. Di Tullio, D. Capitani, F. Presciutti, G. Gentile, B.G. Brunetti, N. Proietti, Non-invasive NMR stratigraphy of a multi-layered artefact: an ancient detached mural painting, Anal Bioanal Chem 405 (2013) 8669–8675. https://doi.org/10.1007/s00216-013-7278-2.
[11] A. Haber, B. Blümich, D. Souvorova, E. Del Federico, Ancient Roman wall paintings mapped nondestructively by portable NMR, Anal Bioanal Chem 401 (2011) 1441–1452. https://doi.org/10.1007/s00216-011-5180-3.
[12] D. Oligschläger, S. Waldow, A. Haber, W. Zia, B. Blümich, Moisture dynamics in wall paintings monitored by single-sided NMR, Magnetic Reson in Chemistry 53 (2015) 48–57. https://doi.org/10.1002/mrc.4153.
[13] N. Proietti, D. Capitani, R. Lamanna, F. Presciutti, E. Rossi, A.L. Segre, Fresco paintings studied by unilateral NMR, Journal of Magnetic Resonance 177 (2005) 111–117. https://doi.org/10.1016/j.jmr.2005.07.015.
[14] N. Proietti, D. Capitani, E. Rossi, S. Cozzolino, A.L. Segre, Unilateral NMR study of a XVI century wall painted, Journal of Magnetic Resonance 186 (2007) 311–318. https://doi.org/10.1016/j.jmr.2007.03.011.
[15] V. Di Tullio, N. Proietti, M. Gobbino, D. Capitani, R. Olmi, S. Priori, C. Riminesi, E. Giani, Non-destructive mapping of dampness and salts in degraded wall paintings in hypogeous buildings: the case of St. Clement at mass fresco in St. Clement Basilica, Rome, Anal Bioanal Chem 396 (2010) 1885–1896. https://doi.org/10.1007/s00216-009-3400-x.
[16] V. Di Tullio, D. Capitani, A. Atrei, F. Benetti, G. Perra, F. Presciutti, N. Proietti, N. Marchettini, Advanced NMR methodologies and micro-analytical techniques to investigate the stratigraphy and materials of 14th century Sienese wooden paintings, Microchemical Journal 125 (2016) 208–218. https://doi.org/10.1016/j.microc.2015.11.036.
[17] N. Marchettini, A. Atrei, F. Benetti, N. Proietti, V. Di Tullio, M. Mascalchi, I. Osticioli, S. Siano, I. Turbanti Memmi, Non-destructive characterisation of fourteenth century painting by means of molecular spectroscopy and unilateral NMR, Surface Engineering 29 (2013) 153–158. https://doi.org/10.1179/1743294412Y.0000000065.
[18] F. Presciutti, J. Perlo, F. Casanova, S. Glöggler, C. Miliani, B. Blümich, B.G. Brunetti, A. Sgamellotti, Noninvasive nuclear magnetic resonance profiling of painting layers, Applied Physics Letters 93 (2008) 033505. https://doi.org/10.1063/1.2963026.
[19] C. Invernizzi, G. Fiocco, M. Iwanicka, M. Kowalska, P. Targowski, B. Blümich, C. Rehorn, V. Gabrielli, D. Bersani, M. Licchelli, M. Malagodi, Non-invasive mobile technology to study the stratigraphy of ancient Cremonese violins: OCT, NMR-MOUSE, XRF and reflection FT-IR

spectroscopy, Microchemical Journal 155 (2020) 104754. https://doi.org/10.1016/j.microc.2020.104754.
[20] N. Proietti, V. Di Tullio, D. Capitani, R. Tomassini, M. Guiso, Nuclear magnetic resonance in contemporary art: the case of “Moon Surface” by Turcato, Appl. Phys. A 113 (2013) 1009–1017. https://doi.org/10.1007/s00339-013-7729-9.
[21] C. Kehlet, A. Catalano, J. Dittmer, Degradation of natural rubber in works of art studied by unilateral NMR and high field NMR spectroscopy, Polymer Degradation and Stability 107 (2014) 270–276. https://doi.org/10.1016/j.polymdegradstab.2013.12.039.
[22] C. Kehlet, E. Del Federico, H. Schahbaz, A. Catalano, J. Dittmer, N.Chr. Nielsen, Non-invasive characterization of polymeric materials in relation to art conservation using unilateral NMR combined with multivariate data analysis, Anal. Methods 5 (2013) 4480. https://doi.org/10.1039/c3ay40650d.
[23] N. Proietti, D. Capitani, E. Pedemonte, B. Blümich, A.L. Segre, Monitoring degradation in paper: non-invasive analysis by unilateral NMR. Part II, Journal of Magnetic Resonance 170 (2004) 113–120. https://doi.org/10.1016/j.jmr.2004.06.006.
[24] N. Proietti, F. Presciutti, V. Di Tullio, B. Doherty, A.M. Marinelli, B. Provinciali, N. Macchioni, D. Capitani, C. Miliani, Unilateral NMR, 13C CPMAS NMR spectroscopy and micro-analytical techniques for studying the materials and state of conservation of an ancient Egyptian wooden sarcophagus, Anal Bioanal Chem 399 (2011) 3117–3131. https://doi.org/10.1007/s00216-010-4229-z.
[25] K. Ulrich, S.A. Centeno, J. Arslanoglu, E. Del Federico, Absorption and diffusion measurements of water in acrylic paint films by single-sided NMR, Progress in Organic Coatings 71 (2011) 283–289. https://doi.org/10.1016/j.porgcoat.2011.03.019.
[26] V. Di Tullio, G. Sciutto, N. Proietti, S. Prati, R. Mazzeo, C. Colombo, E. Cantisani, V. Romè, D. Rigaglia, D. Capitani, 1H NMR depth profiles combined with portable and micro-analytical techniques for evaluating cleaning methods and identifying original, non-original, and degraded materials of a 16th century Italian wall painting, Microchemical Journal 141 (2018) 40–50. https://doi.org/10.1016/j.microc.2018.04.034.
[27] G.R. Fife, B. Stabik, A.E. Kelley, J.N. King, B. Blümich, R. Hoppenbrouwers, T. Meldrum, Characterization of aging and solvent treatments of painted surfaces using single-sided NMR, Magnetic Reson in Chemistry 53 (2015) 58–63. https://doi.org/10.1002/mrc.4164.
[28] P. Moretti, L. Cartechini, C. Miliani, Single-sided NMR: a non-invasive diagnostic tool for monitoring swelling effects in paint films subjected to solvent cleaning, Anal Bioanal Chem 412 (2020) 1063–1075. https://doi.org/10.1007/s00216-019-02331-x.
[29] R. Nicasy, H. Huinink, B. Erich, A. Olaf, NMR Profiling of Reaction and Transport in Thin Layers: A Review, Polymers 14 (2022) 798. https://doi.org/10.3390/polym14040798.
[30] B. Blümich, S. Haber-Pohlmeier, W. Zia, Compact NMR, De Gruyter, Berlin Boston, 2014.
[31] C. Thillaye Du Boullay, M. Jaber, M. Le Denic, F. Gerony, R. Bordes, G. Mériguet, A.-L. Rollet, P. Walter, L. De Viguerie, On the way to tempera grassa: Unraveling the properties of emulsion-based paint binders, Colloids and Surfaces A: Physicochemical and Engineering Aspects 673 (2023) 131816. https://doi.org/10.1016/j.colsurfa.2023.131816.
[32] H.Y. Carr, E.M. Purcell, Effects of Diffusion on Free Precession in Nuclear Magnetic Resonance Experiments, Phys. Rev. 94 (1954) 630–638. https://doi.org/10.1103/PhysRev.94.630.
[33] F. Casanova, J. Perlo, NMR in Inhomogeneous Fields, in: F. Casanova, J. Perlo, B. Blümich (Eds.), Single-Sided NMR, Springer Berlin Heidelberg, Berlin, Heidelberg, 2011: pp. 11–56. https://doi.org/10.1007/978-3-642-16307-4_2.
[34] A. Traoré, C. Rondeau-Mouro, R. Aliouissi, A. Benmoussa, J.-M. Bonny, G. Pagès, Profiling the temperature dependent frequency of an open-magnet for outdoor applications, (2019). hal-02735518.
[35] Z. Cai, Inverse Laplace Transform of Real-valued Relaxation Data by a Regularized Non-negative Least Squares Method, (2019). https://github.com/caizkun/pyilt.
[36] F. Crameri, Scientific colour maps, (2023). https://doi.org/10.5281/ZENODO.1243862.

[37] F. Crameri, G.E. Shephard, P.J. Heron, The misuse of colour in science communication, Nat Commun 11 (2020) 5444. https://doi.org/10.1038/s41467-020-19160-7.
[38] https://gitlab.com/soleil-psiche/tomodata, (n.d.).
[39] A. King, N. Guignot, P. Zerbino, E. Boulard, K. Desjardins, M. Bordessoule, N. Leclerq, S. Le, G. Renaud, M. Cerato, M. Bornert, N. Lenoir, S. Delzon, J.-P. Perrillat, Y. Legodec, J.-P. Itié, Tomography and imaging at the PSICHE beam line of the SOLEIL synchrotron, Review of Scientific Instruments 87 (2016) 093704. https://doi.org/10.1063/1.4961365.
[40] A. King, N. Guignot, J.-P. Deslandes, M. Pelerin, I. Joosten, D. De Looff, J. Li, L. Bertrand, E. Rosenberg, A. Dewaele, E. Boulard, Y. Le Godec, J.-P. Perrillat, E. Giovenco, G. Morard, T. Weitkamp, M. Scheel, J. Perrin, H. Chevreau, J.-P. Itié, Recent Tomographic Imaging Developments at the PSICHE Beamline, Integr Mater Manuf Innov 8 (2019) 551–558. https://doi.org/10.1007/s40192-019-00155-2.
[41] J. Schindelin, I. Arganda-Carreras, E. Frise, V. Kaynig, M. Longair, T. Pietzsch, S. Preibisch, C. Rueden, S. Saalfeld, B. Schmid, J.-Y. Tinevez, D.J. White, V. Hartenstein, K. Eliceiri, P. Tomancak, A. Cardona, Fiji: an open-source platform for biological-image analysis, Nat Methods 9 (2012) 676–682. https://doi.org/10.1038/nmeth.2019.
[42] C. Guérin-Dubiard, J.-L. Audic, Egg-Protein-Based Films and Coatings, in: Huopalahti, R., López-Fandiño, R., Anton, M., Schade, R. (Eds) Bioactive Egg Compounds, Springer, Berlin, 2007: pp. 1–6.
[43] C.J. Brinker, G.W. Scherer, Drying, in: Sol-Gel Science: The Physics and Chemistry of Sol–Gel Processing, Academic Press, Elsevier, Cambridge, 1990: pp. 452–513. https://doi.org/10.1016/B978-0-08-057103-4.50013-1.
[44] P. Bacchin, D. Brutin, A. Davaille, E. Di Giuseppe, X.D. Chen, I. Gergianakis, F. Giorgiutti-Dauphiné, L. Goehring, Y. Hallez, R. Heyd, R. Jeantet, C. Le Floch-Fouéré, M. Meireles, E. Mittelstaedt, C. Nicloux, L. Pauchard, M.-L. Saboungi, Drying colloidal systems: Laboratory models for a wide range of applications, Eur. Phys. J. E 41 (2018) 94. https://doi.org/10.1140/epje/i2018-11712-x.
[45] L. Pauchard, Evolution of colloidal coatings due to a wetting and drying process, Physics of Fluids 35 (2023) 067107. https://doi.org/10.1063/5.0153415.
[46] L. Xu, Y. Zhao, M. Xu, X. Nie, N. Wu, Y. Tu, Formation mechanism of low-density lipoprotein gel induced by NaCl, Poultry Science 98 (2019) 5166–5176. https://doi.org/10.3382/ps/pez232.
[47] Y. Zhao, F. Feng, Y. Yang, C. Xiong, M. Xu, Y. Tu, Gelation behavior of egg yolk under physical and chemical induction: A review, Food Chemistry 355 (2021) 129569. https://doi.org/10.1016/j.foodchem.2021.129569.
[48] M. Anton, Egg yolk: structures, functionalities and processes: Egg yolk: structures, functionalities and processes, J. Sci. Food Agric. 93 (2013) 2871–2880. https://doi.org/10.1002/jsfa.6247.
[49] R. Jayasundar, S. Ayyar, P. Raghunathan, Proton resonance imaging and relaxation in raw and cooked hen eggs, Magnetic Resonance Imaging 15 (1997) 709–717. https://doi.org/10.1016/S0730-725X(97)00010-6.
[50] S. Sfakianaki, Egg yolk identification and aging in mixed paint binding media by NMR spectroscopy, Magn. Reson. Chem. (2015).
[51] S.M. Ackermann, D.W. Lachenmeier, T. Kuballa, B. Schütz, M. Spraul, M. Bunzel, NMR-based differentiation of conventionally from organically produced chicken eggs in Germany, Magn Reson Chem 57 (2019) 579–588. https://doi.org/10.1002/mrc.4838.
[52] F. Gerony, A. Fanost, R.T. Zlanseu, N. Malikova, L. Michot, M. Poirier-Quinot, L. De Viguerie, M. Jaber, G. Mériguet, A.-L. Rollet, Structural and dynamical impact of water dilution on egg yolk properties, (2025). https://doi.org/10.26434/chemrxiv-2025-5t6t2.
[53] K. Poznańska, A. Hola, R. Kozłowski, M. Strojecki, Ł. Bratasz, Mechanical and moisture-related properties of selected dried tempera paints, Herit Sci 12 (2024) 25. https://doi.org/10.1186/s40494-024-01147-y.

[54] T. Überrück, C. Rehorn, R. Höhner, B. Blümich, Visualizing the detection area of a unilateral NMR sensor using deconvolution and back-projection, Journal of Magnetic Resonance 296 (2018) 169–175. https://doi.org/10.1016/j.jmr.2018.09.007.
[55] L. Laghi, M.A. Cremonini, G. Placucci, S. Sykora, K. Wright, B. Hills, A proton NMR relaxation study of hen egg quality, Magnetic Resonance Imaging 23 (2005) 501–510. https://doi.org/10.1016/j.mri.2004.12.003.
[56] A. Fanost, L. Viguerie, G. Ducouret, G. Mériguet, P. Walter, H. Glanville, A. Rollet, M. Jaber, Connecting Rheological Properties and Molecular Dynamics of Egg-Tempera Paints based on Egg Yolk, Angewandte Chemie Intl Edit 61 (2022). https://doi.org/10.1002/anie.202112108.
[57] B. Hills, S. Benamira, N. Marigheto, K. Wright, T1-T2 correlation analysis of complex foods, Appl. Magn. Reson. 26 (2004) 543–560. https://doi.org/10.1007/BF03166582.
[58] C. Au, T. Wang, N.C. Acevedo, Development of a low resolution 1H NMR spectroscopic technique for the study of matrix mobility in fresh and freeze-thawed hen egg yolk, Food Chemistry 204 (2016) 159–166. https://doi.org/10.1016/j.foodchem.2016.02.085.
[59] Y. Kharbanda, S. Mailhiot, O. Mankinen, M. Urbańczyk, V.-V. Telkki, Monitoring cheese ripening by single-sided nuclear magnetic resonance, Journal of Dairy Science 106 (2023) 1586–1595. https://doi.org/10.3168/jds.2022-22458.
[60] M. Anton, Composition and Structure of Hen Egg Yolk, in: Huopalahti, R., López-Fandiño, R., Anton, M., Schade, R. (Eds) Bioactive Egg Compounds, Springer, Berlin, 2007: pp. 1–6.
[61] J.V. Koleske, Drying Oils, in: J.V. Koleske (Ed.), Paint and Coating Testing Manual: 15th. Edition of the Gardner-Sward Handbook, ASTM International, 100 Barr Harbor Drive, PO Box C700, West Conshohocken, PA 19428-2959, 2012: pp. 32–37. https://doi.org/10.1520/MNL12184M.
[62] F. Gerony, L. De Viguerie, C.T. Du Boullay, F. Gaslain, B. Lanson, C. Colin, L. Michot, A.-L. Rollet, G. Mériguet, M. Jaber, Diving into micro- and macroscopic properties of egg-tempera paint based on Sienna pigment, Applied Clay Science 249 (2024) 107236. https://doi.org/10.1016/j.clay.2023.107236.
[63] M. Rooney, T. Meldrum, Effect of pigment concentration on NMR relaxometry in acrylic paints, Magnetic Reson in Chemistry 58 (2020) 880–888. https://doi.org/10.1002/mrc.5053.
[64] L. Kiple, T. Lee, G. Zavaglia, T. Meldrum, Characterization of molecular environments and chemical exchange in acrylic paints via single-sided NMR, Progress in Organic Coatings 183 (2023) 107770. https://doi.org/10.1016/j.porgcoat.2023.107770.
[65] F. Busse, C. Rehorn, M. Küppers, N. Ruiz, H. Stege, B. Blümich, NMR relaxometry of oil paint binders, Magn Reson Chem 58 (2020) 830–839. https://doi.org/10.1002/mrc.5020.
[66] R.J. Meilunas, J.G. Bentsen, A. Steinb, Analysis of Aged Paint Binders by FTIR Spectroscopy, STUD CONSERV 35 (1990) 20. https://doi.org/10.2307/1506280.
[67] M. Odlyha, N.S. Cohen, G.M. Foster, R.H. West, Dosimetry of paintings: determination of the degree of chemical change in museum exposed test paintings (azurite tempera) by thermal and spectroscopic analysis, Thermochimica Acta 365 (2000) 53–63. https://doi.org/10.1016/S0040-6031(00)00613-4.
[68] N.A. Udell, R.E. Hodgkins, B.H. Berrie, T. Meldrum, Physical and chemical properties of traditional and water-mixable oil paints assessed using single-sided NMR, Microchemical Journal 133 (2017) 31–36. https://doi.org/10.1016/j.microc.2017.03.013.
[69] M. Du, D.U. Ahn, J.L. Sell, Effect of dietary conjugated linoleic acid on the composition of egg yolk lipids, Poultry Science 78 (1999) 1639–1645. https://doi.org/10.1093/ps/78.11.1639.
[70] A.A. Coelho, *TOPAS* and *TOPAS-Academic*: an optimization program integrating computer algebra and crystallographic objects written in C++, J Appl Crystallogr 51 (2018) 210–218. https://doi.org/10.1107/S1600576718000183.

Funding sources

This work was supported by the *Observatoire des Patrimoines de l'Alliance Sorbonne Universit*é (OPUS).

Acknowledgments

The authors wish to acknowledge Andrew King from SOLEIL for the beamtime of synchrotron on the PSICHÉ beamline. The authors want to thank Françoise Pillier for the SEM analysis.

Author contributions: CRediT

Floriane Gerony: Conceptualization, Resources, Methodology, Formal analysis, Investigation, Data Curation, Writing - Original Draft, Visualization, Project administration
Côme Thillaye du Boullay: Methodology, Software, Formal analysis, Data Curation, Writing - Review & Editing
Laurence de Viguerie: Conceptualization, Methodology, Writing - Review & Editing, Supervision
Laurent Michot: Methodology, Writing - Review & Editing, Supervision
Pauline Martinetto: Investigation, Formal analysis
Maïwenn Le Denic: Investigation
Rémi Brageu: Investigation
Thiéry Guillou: Resources
Anne-Laure Rollet : Conceptualization, Methodology, Writing - Original Draft, Writing - Review & Editing, Validation, Supervision
Maguy Jaber : Conceptualization, Writing - Review & Editing, Funding acquisition, Supervision, Project administration
Guillaume Mériguet : Conceptualization, Validation, Formal analysis, Writing - Original Draft, Writing - Review & Editing, Supervision, Project administration

Supplementary Information:

S1. Drying speeds

The mass of the egg yolk and tempera films was monitored during drying (Figure S1). The mass loss was normalized by the maximum mass. Similarly, the signal amplitude on the total thickness of the film, related to the number of protons, is shown in Figure S2. The derivatives of these signals (in gray) allow us to measure the evolution of loss speeds over time. It can be seen that mass loss is immediate, while proton loss, measured at the center of the film, is slightly offset in time as drying starts at the edges. The mass loss corresponds to the amount of water in the film, while the proton loss is greater because the least mobile protons are not detected.

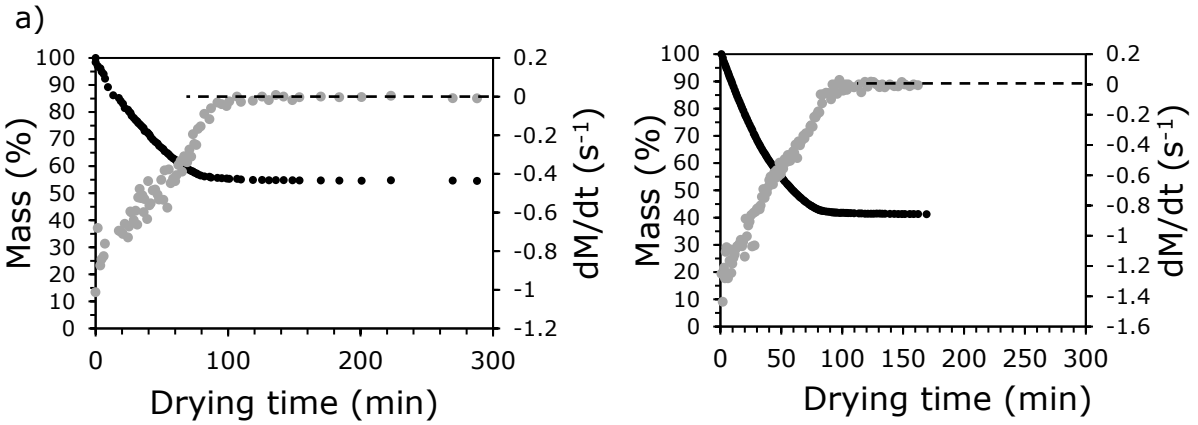

Figure S1: Mass loss and mass derivation during drying of egg yolk (a) and tempera (b) films.

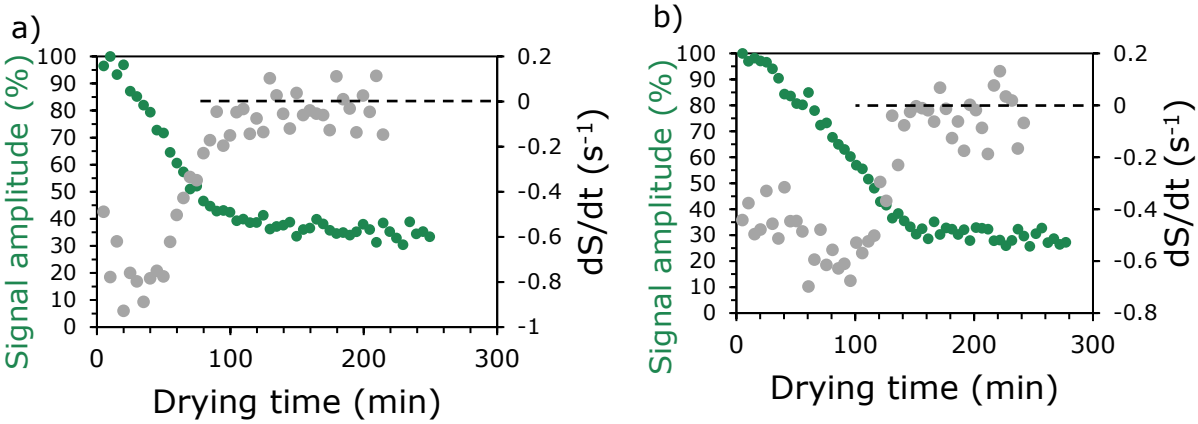

Figure S2: Signal amplitude loss and signal derivation during drying of egg yolk (a) and tempera (b) films. The signal is smoothed using the 6-point moving average method before the derivative is calculated.

S2. Estimation of deviation between samples

The drying of egg yolk films has been recorded several times at different times of the year. For the same egg supplier, hen feed may vary, affecting yolk composition [69]. Measurement conditions (ambient temperature and humidity) can also affect drying time. However, the measured relaxation

times are very close, as shown by the fine error bars (Figure S3). Thus, we can consider that even the small differences are significant.

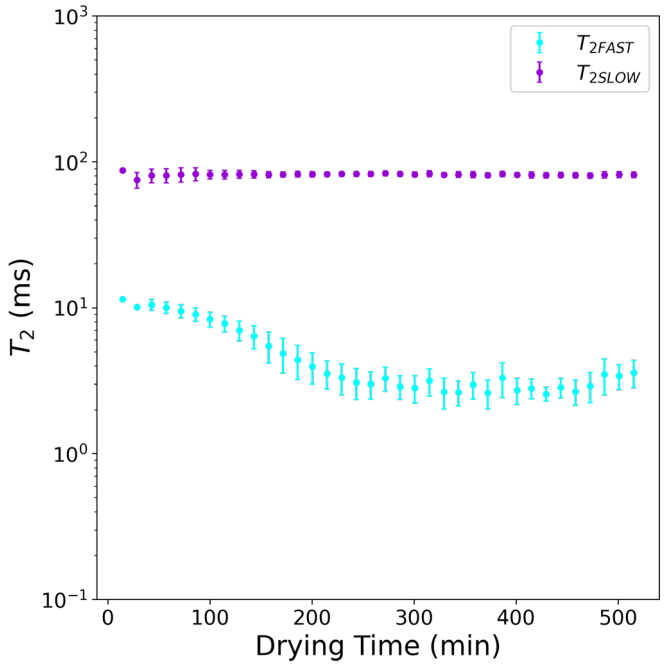

Figure S3: Mean and standard deviation of the transverse relaxation times (T_2) obtained during drying of three films of egg yolk (500 µm thick) at different time of the year (September 2022, January 2023 and May 2024).

S3. Pigment characterization

Lead-tin yellow (type I) and azurite pigment have been characterized here after, whereas precise characterization of sienna is available in another paper [62].

Methods

Pycnometry

Density measurements were carried out using a ~25 mL glass pycnometer (the exact volume of which was measured by taking the mass of the distilled water that occupies it). Approximately 1g of pigment powder was introduces and the volume was completed with distilled water at 21°C, taking care not to create any bubbles and wiping well the exterior.

X-Ray Powder Diffraction (XRPD)

X-ray powder diffraction patterns of pigments were obtained with a Bruker D8 Discover diffractometer with a non-monochromated Cu Kα radiation (40 kV, 30 mA) as the X-ray source. The scanning range was 5-120° (2θ) with a step size of 0.01° and an integration time of 3 s for each step. Rietveld refinements were performed with TOPAS software [70].

Scanning Election Microscopy (SEM)

SEM images of powder pigments were obtained with a SEM-FEG ZEISS ultra 55 at 10 kV. Sample topography was observed using secondary electron detection: In-Lens or Everhart Thornley-type SE detector for lead-tin yellow and azurite, respectively.

Results

Lead-Tin Yellow type I

Density: 8.1

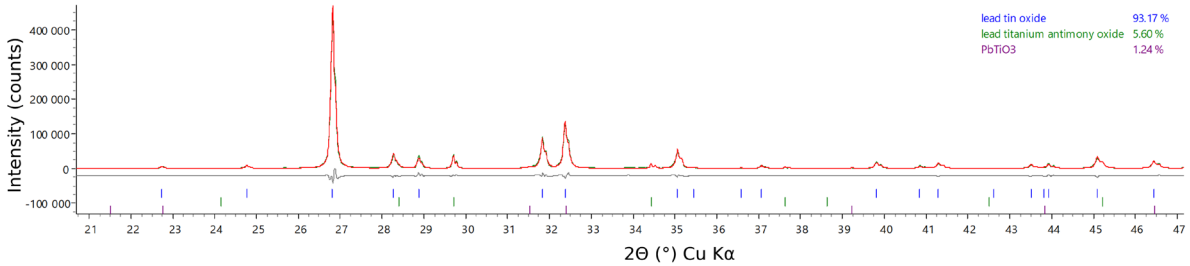

	Pb_2SnO_4	$Pb_2TiSbO_{6.5}$	$PbTiO_3$
Jaune de plomb étain type I (Rwp = 10.8)	93.2 (0.1)	5.6 (0.1)	1.2 (0.1)

Figure S4: XRD diagram and Rietveld refinement of lead-tin yellow type I.

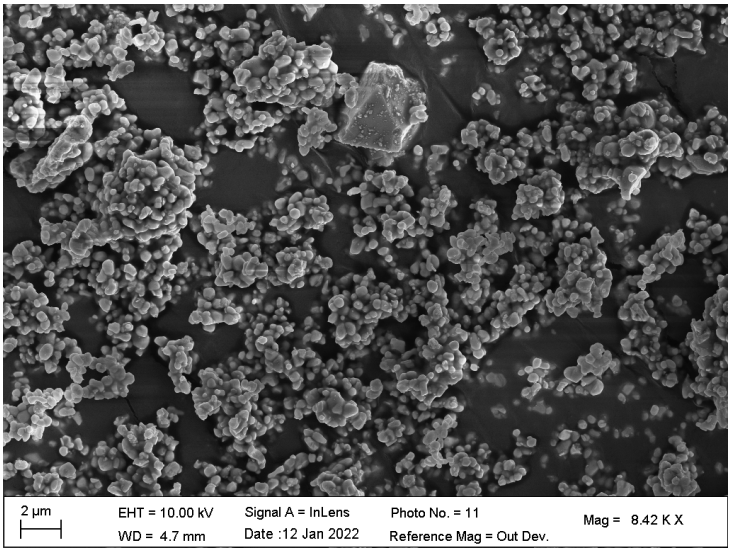

Figure S5: SEM image of lead-tin yellow pigment.

Azurite

Density: 3.5

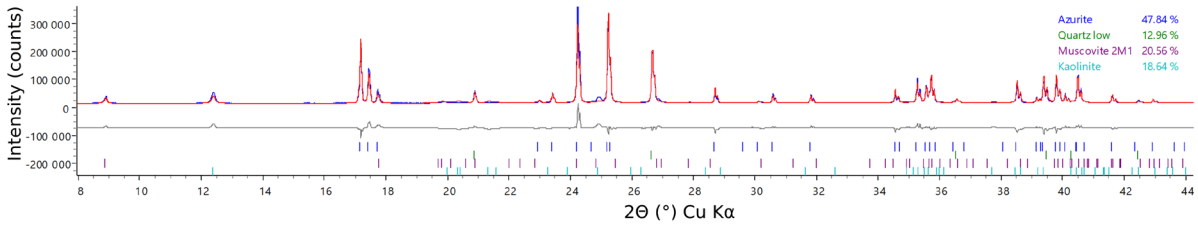

	Kaolinite	Quartz	Muscovite	Azurite $Cu_3(CO_3)_2(OH)_2$
Azurite (Rwp = 6.2)	18.6 (0.6)	13.0 (0.2)	20.6 (0.7)	47.8 (0.5)

Figure S6: XRD diagram and Rietveld refinement of azurite pigment.

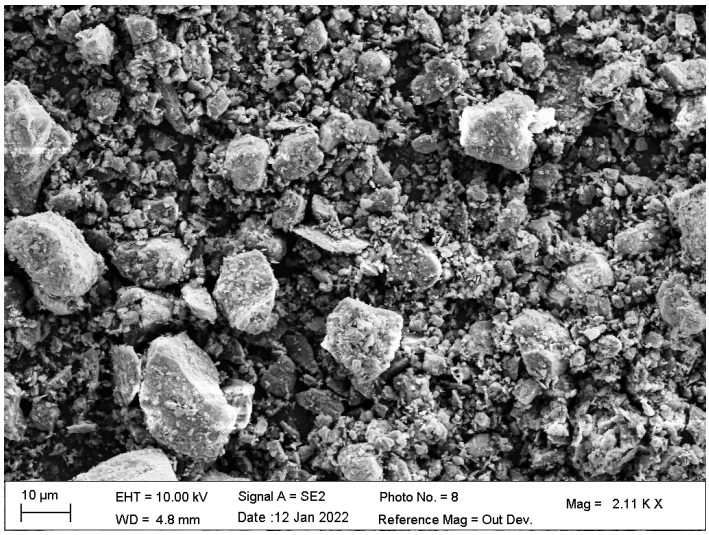

Figure S7: SEM image of azurite pigment.

S4. Pigment sedimentation observed in the dry films

Measurements to monitor drying must be carried out quickly, and therefore require a limited number of scans. We therefore carried out a second series of measurements on the dried films, with better resolution (10 µm instead of 20 µm) and more acquisitions (400 scans instead of 12), which considerably improves the signal-to-noise ratio. These measurements were also made several times and at different points on the films to ensure reproducibility (Figure S8). This enabled us to obtain a precise profile, and in particular to distinguish a thickness of around ten microns less dense in protons at the surface of the glass slide on lead-tin yellow and azurite-based films. This is attributed to the layer of sedimented pigment particles visible at the bottom of the fresh paint bottles (Figure 10). The profiles of Sienna-based films do not show a shoulder, but do have an irregular profile, suggesting that the pigment is not evenly distributed throughout the depth of the film.

In the photo of the azurite-based film (Figure S9 b), the central zone, which corresponds to that scanned by the instrument during drying, looks different from the rest of the film. This zone is lighter on the surface, and its profile (Figure S8 5) is different: thicker, with a ^{1}H-dense layer on the surface. We can therefore hypothesize that the heat generated by the coil during the experiment influences the drying process, possibly by generating convection flows and/or surface bubbles. Also, the magnetic field generated by the magnet may alter the position of particles in the film (attracting them towards the bottom) and contribute to the inhomogeneity observed.

Another azurite-based paint film was prepared 6 months later, dried outside the instrument, and does not show the zone described above (Figure S9 a). This also highlights the discoloration of the films after 6 months of exposure to natural light.

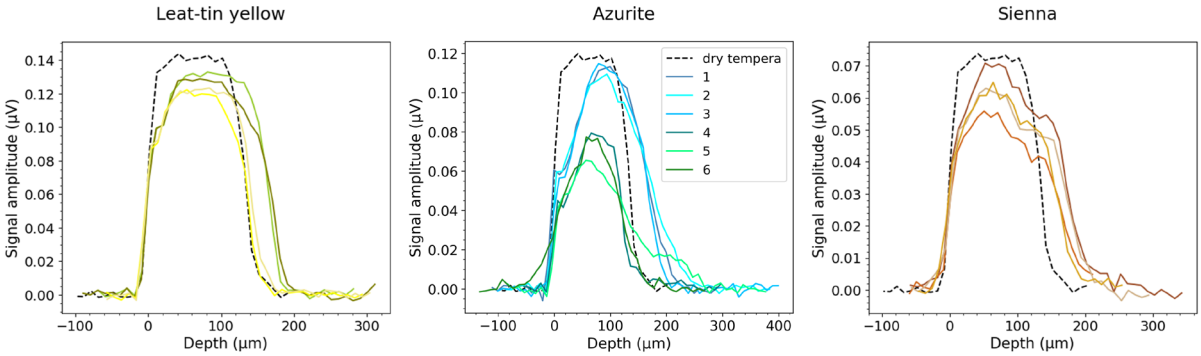

Figure S8: Profiles of dry films. The azurite-based film profiles are numbered according to the area scanned (see Figure S9). For comparison of the shape of the glass slide - film interface, the normalized profile of the dry tempera film is plotted.

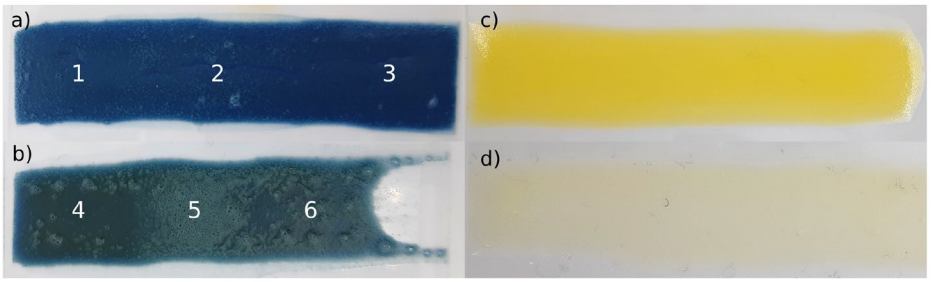

Figure S9: Photographs of dry films before and after 6 months of exposition to natural light. Azurite tempera paint film (a) fresh and (b) aged, and pure egg yolk film (c) fresh and (d) aged. The numbers on the azurite films correspond to the profile acquisition zones in Figure S8.